2016-01-0593

Cycle-to-Cycle Variations in Multi-Cycle Engine RANS Simulations

Author, co-author (Do NOT enter this information. It will be pulled from participant tab in MyTechZone)

Affiliation (Do NOT enter this information. It will be pulled from participant tab in MyTechZone)

Abstract

Reynolds-averaged Navier-Stokes (RANS) modeling is expected to deliver an ensemble-averaged result for the majority of turbulent flows. This could lead to the conclusion that multi-cycle internal combustion engine (ICE) simulations performed using RANS must exhibit a converging numerical solution after a certain number of consecutive cycles. However, for some engine configurations unsteady RANS simulations are not guaranteed to deliver an ensemble-averaged result.

In this paper it is shown that, when using RANS modeling to simulate multiple engine cycles, the cycle-to-cycle variations (CCV) generated from different initial conditions at each cycle are not damped out even after a large number of cycles. A single-cylinder GDI research engine is simulated using RANS modeling and the numerical results for 20 consecutive engine cycles are evaluated for two specific operating conditions. One condition is characterized by stoichiometric operation and stable combustion ($COV_{IMEP} < 2\%$) and the other features dilute combustion resulting in misfire events and much higher COV_{IMEP}. In both cases, multi-cycle RANS simulation results show cyclic variability.

An in-depth analysis of the most significant physical and chemical quantities highlights that CCV are caused primarily by the variability of the in-cylinder flow. For stoichiometric combustion this does not greatly affect flame propagation, and the resulting fluctuations of the pressure traces are narrow. However, in the event of dilute combustion, the variability of the flow gains more importance, therefore delivering large cyclic fluctuations of in-cylinder pressure. Even though unsteady RANS simulations are not expected to predict as much variability in engine flows as LES, in particular for stable cases, they can still be used to capture typical combustion stability features in an internal combustion engine.

This paper shows that the occurrence of CCV when using multi-cycle RANS modeling is not a numerical artifact or the effect of changes in the computational grid from cycle to cycle. Cold-flow analysis reveals that the variability of the simulated flow is intrinsic for the unsteady RANS approach and can only be damped out by increasing numerical viscosity, either by increasing the cell size or by adding up-winding. This is proved in a simplified non-ICE case such as the simulation of the vortex shredding from a cylinder in cross flow. Also, the effect of numerical viscosity on CCV is shown for multi-cycle engine simulations by using a simplified combustion model. Finally, it is shown that multi-cycle RANS can successfully predict the effect of changing specific engine parameters, such as the properties of the ignition system, on cyclic variability and combustion stability.

Introduction

Due to the U.S. heavy reliance on gasoline internal combustion engines (ICEs) for automotive transportation, efficiency improvements of advanced gasoline spark-ignition (SI) combustion concepts have the potential to dramatically reduce oil consumption and CO_2 emissions. To this aim, increasing effort is being put into investigating advanced dilute gasoline combustion concepts to enable further efficiency gains [1]. The most common ways to achieve dilute combustion are: 1) burning mixture containing oxygen in excess (lean-burn) or 2) using exhaust gas recirculation (EGR). However dilute combustion, be it lean or EGR, deteriorates combustion stability, thus limiting the efficiency improvements. Recent studies from the authors focused on lean and EGR-dilute combustion in a GDI engine to characterize combustion stability [2].The most common measure of combustion stability is the coefficient of variation (COV) of the indicated mean effective pressure (IMEP), COV_{IMEP}, defined as the standard deviation of IMEP (σ_{IMEP}) divided by the mean value of IMEP (μ_{IMEP}). When comparing dilute combustion to non-dilute operation, the engine exhibited large variations of the IMEP from cycle to cycle that could be attributed to the increase in ignition delay and combustion duration.

Computational Fluid Dynamics (CFD) has proved to be an effective tool for the analysis of internal combustion engines and undergoes constant development with the goal of improving the accuracy of numerical results. Reynolds Averaged Navier-Stokes (RANS) simulations are widely used, especially in industry, due to relatively low computational power requirements. Large Eddy Simulation (LES) results have been shown in the last decade to improve the accuracy of engine simulations and introduce a stochastic analysis of the physical processes within the engine itself. When comparing RANS to LES, it is common opinion to consider LES as the only way to capture unsteady engine behavior. RANS is typically characterized by a higher spatial filter than LES. Therefore it is certainly less accurate than LES, since the latter can capture flow structures at smaller scales.

The internal combustion engine does not operate at steady state as each cycle is different from the previous and next cycle. Therefore it is not clear that multi-cycle RANS results should converge to an ensemble-solution after a certain number of cycles. In some cases, the large flow structures may change from cycle to cycle due to the fact that the initial conditions do not necessarily repeat. Also, the effect of those variations on flame propagation is not obvious, because it depends on the flame speed itself. Nevertheless, in most of the published work on engine multi-dimensional modeling, LES is considered as the only approach capable to show cyclic variability in an engine, while RANS is expected to deliver a cycle-based average result.

Vermorel et al. [3] showed that with only 9 cycles of LES it was possible to qualitatively capture the observed cyclic variability in a spark-ignition (SI) engine fueled with propane. Enaux et al. [4] extended their analysis up to 25 consecutive cycles for an operating conditions characterized by low cycle-to-cycle variations (CCV). Granet et al. [5] further extended the previous analysis and concluded that: 1) LES was able to distinguish stable and unstable operating conditions; 2) 25 consecutive LES cycles were necessary to capture the CCV trend for the stable condition; 3) 50 consecutive LES cycles were necessary to capture the CCV trend for the unstable condition. Tatschl et al. [6] recently showed 20 consecutive LES cycles and explained the CCV phenomenon emphasizing the large variability of the flow in the near spark region. Koch et al. [7] investigated the effect of mesh resolution on CCV and ran up to 40 consecutive cycles

showing significant variations of the sub-grid turbulent kinetic energy for different mesh sizes. Fontanesi et al. [8] recently compared RANS and LES for the same operating condition, characterized by relatively stable combustion, in a turbo-charged GDI engine, running the simulations for 10 consecutive cycles. Very small fluctuations of the numerical pressure trace were observed with RANS and were related to slight changes of trapped mass for each cycle. Larger fluctuations were observed with LES although the amplitude between minimum and maximum numerical pressure traces did not match the experimental data. Also, they clearly showed that using average pressure conditions for the intake and exhaust boundaries did not alter the numerical cyclic variability. Goryntsev at el. [9] have also extensively investigated unsteady effects in direct injection spark ignition (DISI) engines and have recently used LES to analyze misfire events.

Two main features can be highlighted in all the above-mentioned studies: 1) they all focus on SI engines only, and 2) they all justify the numerical cyclic variability with the changes in the flow configuration from cycle to cycle, especially in the near spark-region. The two features are strongly correlated: it is in fact well known that the mixture and flow properties in the proximity of the spark location have significant impact on the early flame propagation process and consequently on the entire combustion process in SI engines [10].

Recent multi-cycle RANS simulations performed by the authors of this paper did not show a converging numerical solution and delivered LES-like results [11,12,13]. Large fluctuations of the numerical pressure traces were shown for both pre-mixed lean [12] and DI EGR-dilute [13] gasoline combustion. Recent work provided an explanation of why RANS does not necessarily deliver an ensemble-average result in ICE as well as non-ICE applications [14]. In particular, the effect of numerical viscosity on the trade-off between accuracy and stability of the numerical solution was investigated. It was shown that fine meshes and high order of numerics are likely to significantly reduce the numerical viscosity to such an extent that the change of initial conditions from cycle to cycle is not damped out even after a relatively large number of consecutive cycles.

This paper expands on our previous investigations on RANS multi-cycle simulations for SI engines and focuses on explaining the source of CCV in multi-cycle RANS simulations. Compared to most recent results [13], the number of consecutive cycles is increased and in-depth analysis of the numerical data is carried out. Selected test cases are presented in this study in order to clarify whether CCV with RANS has a physical meaning or is just the result of a numerical artifact. The key role played by numerical viscosity in affecting numerical repeatability is highlighted in both ICE and non-ICE applications. Furthermore, two different combustion models are shown to reproduce the same effect in terms of cyclic variability, thus demonstrating that choice of the combustion model is not relevant to the purpose of this paper. Combustion stability is investigated in EGR dilute as well as non-dilute GDI operation, and the comparison between two ignition strategies is carried out both experimentally and numerically.

Experimental Setup

The experimental tests discussed in this paper were carried out on a single-cylinder research engine coupled to a dynamometer intended for steady-state operation. The engine design is representative of a modern GDI engine used for automotive applications. Engine specifications are listed in Table 1. The engine has a 4-valve, 40° pent roof combustion chamber design with central spark plug and injector. It also has a pressure transducer port fitted with an AVL GU21C for high-speed in-cylinder data acquisition. Intake and exhaust ports are fitted with Kulite ETL-179B-190M-2BarA and Kulite EWCT-312M-3.5BarA sensors respectively for high speed pressure data which are used as boundary conditions for 3D-CFD simulations. Compressed air is supplied to the test cell and used as combustion air for boosted as well as throttled engine operation, although the 2000 RPM, 6 bar IMEP operating point examined in this study is throttled exclusively. Between the intake and the exhaust is a cooled EGR loop. It is connected immediately downstream of the exhaust port and as such is considered high pressure EGR. A precisely positioned poppet valve (along with the respective intake and exhaust pressure) controls the EGR mass flow rate. Exhaust gases pass through a heat exchanger supplied with engine coolant at 85 °C which does the majority of cooling before it passes through a section of stainless steel tubing in open air where some additional cooling takes place. The combination of these two effects maintains the EGR temperature below 85 °C as it enters the intake surge tank. The EGR rate is measured using high range and low range CO2 analyzers sampling from the exhaust and intake respectively. The intake sample is drawn downstream of the EGR loop using a perforated sample probe to ensure that fresh air and EGR are well mixed.

Table 1 Specifications of the single cylinder GDI engine

Displacement	0.626 L
Bore	89.04 mm
Stroke	100.6 mm
Compression Ratio	12.1 : 1
Intake Valve MOP	100 °CA ATDC
Exhaust Valve MOP	255 °CA ATDC
GDI Injector*	6 hole, solenoid
Injection Pressure	150 bar
Spark system	Coil-based, 0.7 mm gap, 75mJ
Fuel	EPA Tier II EEE

*Ford P/N CJ5Z-9F593-A

Two operating conditions were studied at 2000 RPM and 6 bar IMEP, one stoichiometric case with no EGR and a stoichiometric case with 18% EGR (dilute). Table 2 lists the main specifications of the two cases examined in this paper.

Table 2 Specifications of the examined test cases

Test Case	1	2
Engine Speed [RPM]	2000	2000
Engine load – IMEP [bar]	6	6
EGR [%]	18	0
Overall relative air fuel ratio, λ	1	1
Start of Injection (SOI) [°CA ATDC]	-300	-300
Duration of Injection (DOI) [°CA]	65	58
Spark Advance (SA) [°CA ATDC]	-40	-24
COV_{IMEP} [%] measured on 500 cycles	8	1.5
COV_{PMAX} [%] measured on 500 cycles	14	8.5

Typical target values of COV_{IMEP} stated in the literature depend on specific applications and are in the range of 2-10% [10] with modern production engines typically at the lower range of this scale (3-5%). As can be seen in Table 2, the EGR-dilute case (Case 1) shows

relatively high COV_{IMEP}. Conversely, the non-dilute case (Case 2) features much lower COV_{IMEP}, less than 2%, and can be generally considered as very stable operation.

CFD Methodology

In this study, RANS numerical simulations are performed using CONVERGE, a general purpose CFD tool that automates the mesh generation process and permits using simple orthogonal grids, locally forced embedding, and the adaptive mesh refinement algorithm (AMR) [15]. In particular, the AMR delivers small grid size where high temperature and velocity gradients are calculated without significantly increasing the total number of computational cells. Unless otherwise specified, in the cases simulated in this paper the base grid is set to 4 mm and additional mesh refinements deliver a local grid size in the order of 0.5 mm during the gas-exchange and combustion phases, and 0.125 mm at the spark plug location during the ignition event. AMR and embedding allow achieving such a high mesh resolution with a maximum cell count of less than 2 million cells. As a result, typical simulations for this study are run on 48 cores with an average computational time of 2.5 days per engine cycle. The computational domain is shown in Figure 1. While the exhaust transducer is located in the proximity of the cylinder block (at a distance of ≈ 30 mm), a large portion of the intake runner (≈ 200 mm in length) is included in the simulations upstream of the cylinder block.

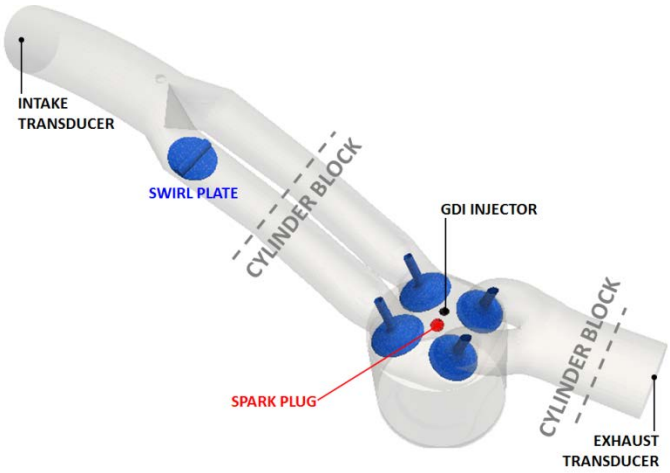

Figure 1 Computational domain used for the simulations shown in this paper

In this paper, multi-cycle simulations are carried out. Previous results [13] showed that with similar grid resolution the calculated in-cylinder pressure trace did not reach convergence even after 10 consecutive cycles. This was explained to be the effect of the low numerical viscosity, achieved using fine mesh and non-diffusive scheme like second order central differencing, which preserves the variability of large-scale eddies from cycle to cycle [14].

Intake and exhaust pressure at the boundaries as well as EGR ratio were measured experimentally and kept constant from cycle to cycle. As far as the GDI spray is concerned, the present study employs the "blob" injection method of Reitz and Diwakar [16], while the atomization of the liquid blobs and subsequent droplets is simulated with models based on the Kelvin-Helmholtz (KH) and Rayleigh-Taylor (RT) instability mechanisms without the use of a breakup length [15]. The No Time Counter (NTC) method of Schmidt and Rutland [17] is used to represent collision between droplets. Detailed sub-models are also included to simulate dynamic drop drag [18] and vaporization [19].

The spark event is simulated through the Eulerian energy deposition model implemented in CONVERGE. The energy from the spark is released to the fluid within a sphere located between the electrodes and the energy transferred is modeled as L-type distribution of the total spark energy to mimic the breakdown and arc/glow phases of the spark discharge. The same approach has shown good accuracy in representing the ignition process for conventional spark-based systems [20]. The total coil energy and the spark event duration used in the simulations were measured experimentally.

Combustion is simulated using the SAGE solver [15] that calculates the reaction rate through detailed chemistry only. Recent work showed that it is possible to simulate flame propagation in SI engines using direct chemistry without turbulence/chemistry interaction (TCI) if a fine mesh is employed, as this significantly reduces the sub-grid effects [21]. Furthermore, the combustion regime for dilute/GDI operation likely falls in the "thickened flame" region in the Borghi's diagram for premixed turbulent combustion [22] as shown in recent CFD papers on SI combustion [12,20]. A detailed mechanism consisting of 110 species and 488 reactions, successfully used to describe gasoline combustion for stoichiometric [11], lean [12], and EGR-dilute [13] operation, is used to describe the chemical reactions involved during the combustion process. In order to speed up the detailed chemistry solutions, the multi-zone model [23] is used during the combustion event. The computational cells are grouped into zones based on temperature and equivalence ratio. A temperature bin size of 5 K is used and an equivalence ratio bin size of 0.05 is used.

It is worth noting that the above-mentioned settings have been extensively validated against engine data for several engine geometries (PFI and GDI, with CR = 10.5 and 12.1 respectively) as well as operating conditions (lean, stoichiometric and stoichiometric with EGR dilution). Moreover, the choice of the specific combustion model is not expected to play a relevant role in delivering or suppressing CCV. However, to add more value to the present study, the analysis of cyclic variability in a real combustion case is carried out using also a different approach for combustion modeling. The level set G-Equation model [24] is used to track the location of the flame front via the transport of the G_EQN passive scalar. When the G-Equation model is used, the G_EQN passive scalar is initialized in the near-spark region to 0.25 mm as recommended (typically twice the minimum local grid-size in the spark region, which is equal to 0.125).

Similarly to what was mentioned about combustion modeling, the choice of the specific spray and ignition models is not expected to alter the results in terms of cyclic variability. In the simulations carried out for this study, as well as in similar multi-cycle simulations with LES, injection and ignition events are assumed to be perfectly repeatable since they are treated in the same identical way for each single cycle. Also, the imposed intake and exhaust boundary conditions, measured using high-speed pressure transducers and low-speed thermo-couples, are identical for each cycle. To give more value to the current analysis it is worth mentioning that the cyclic variations of the measured pressure boundary conditions are minimal. Furthermore, previous work with LES has shown that using average pressure boundaries has no effect on the numerical predictions of cyclic variability [8].

The only perturbation purposely introduced by the authors concerns the re-initialization of the chemical species before the exhaust valve opening (EVO) of each cycle. Using a large mechanism leads to long computational time during the gas exchange phase, and in particular

during the exhaust stroke, due to the fact that transport equations for many species are solved together with significant temperature and velocity gradients. Therefore, prior to EVO, most of the intermediate species are automatically converted to fuel (iso-octane) and only few significant species are preserved. This perturbation in the equivalence ratio of the residual gas is minimal and leads to a cyclic perturbation of the equivalence ratio which is much lower than 1%.

Results and Discussion

Numerical results are organized into seven main sections. First, multi-cycle RANS results for GDI dilute combustion are shown, highlighting large cyclic variability. Detailed discussion is carried out to explain the reason for such variability, with an in-depth analysis of the main physical quantities affecting combustion. Secondly, an additional investigation is carried out to demonstrate that AMR is not the cause of cyclic variability. Third, the cyclic variability of the flow is shown to be an intrinsic property of internal combustion engines. This is done on a cold flow simulation case, i.e. combustion is suppressed. Then, the multi-cycle RANS results are shown for a stoichiometric non-dilute cases highlighting different combustion behavior with respect to the dilute case, despite the fact that the cold flow characteristics are similar for the two cases. The fifth section describes the effect of numerical viscosity on the trade-off between accuracy and repeatability, thus explaining why multi-cycle RANS simulations could still deliver converging pressure traces if the simulation is carried out with higher numerical viscosity. In the same section, a simple example of a cylinder in cross flow is shown to reinforce the previous statement. The sixth section again shows the effect of numerical viscosity on CCV, but uses a different approach for combustion modeling (G-equation) and aims at demonstrating that, using RANS, CCV occurs regardless from the specific combustion model. Finally, the last section shows that multi-cycle RANS results are consistent with engine data and can qualitatively capture typical combustion stability trends.

Section 1: Analysis of multi-cycle RANS results for dilute combustion

Figure 2 shows the numerical results of the multi-cycle RANS simulation for Case 1 (EGR = 18%). As can be seen, the numerical pressure trace features large cyclic fluctuations and a clear no-convergence pattern even after more than 20 consecutive cycles. Typical high-low patterns can also be clearly detected. Figure 3 shows that all the numerical traces fit well within the experimental data, with a noticeable tendency towards below-average cycles.

The RANS approach used in this study delivers numerical results that are very similar to what is shown in literature by using LES. Such a large cyclic variability is not expected using RANS. However, it is worth noting that Case 1 is characterized by a value of the COV_{IMEP} of about 8%, measured over 500 cycles, and presence of misfires, which indicates that combustion is not stable under such dilute conditions. This is a challenging operating condition for RANS calculations and there is not extensive data available in literature using RANS to simulate extremely dilute combustion.

The numerical trend in Figure 2 (and Figure 3) seems to qualitatively describe large CCV and typical features of low combustion stability. Nevertheless it is mandatory to understand where the cyclic variability of the RANS results comes from and whether it has physical meaning.

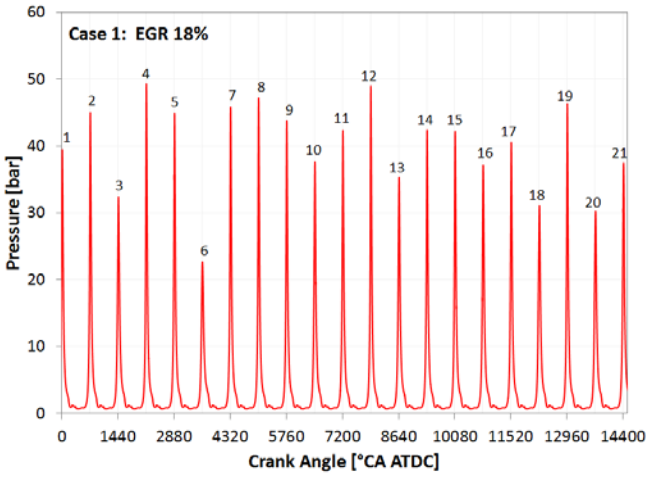

Figure 2 Numerical pressure traces for Case 1

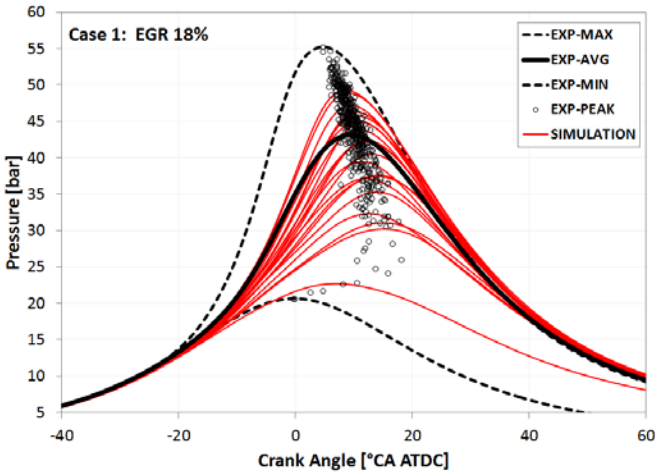

Figure 3 Comparison between numerical and experimental pressure traces for Case 1 (21 simulated cycles vs. 500 experimental cycles)

Figure 4 shows the cycle-resolved calculation of the total mass trapped in the cylinder (the term "GLOBAL" indicates the average value over the entire cylinder). Values shown in Figure 4 are calculated at the time of the spark event. The most relevant difference that can be detected occurs between the first and second cycle. This is expected since the calculation for the first simulation cycle is greatly affected by the initial conditions and the results for this cycle should not be considered. After the first cycle, the trapped mass slightly oscillates and does not converge to a constant value, nevertheless such fluctuations are very low (less than 0.5%) and cannot be itself the cause for the cyclic variability of the numerical results. It is worth mentioning that the in-cylinder pressure and temperature values (not reported here for sake of brevity) follow a similar trend to the one shown in Figure 4.

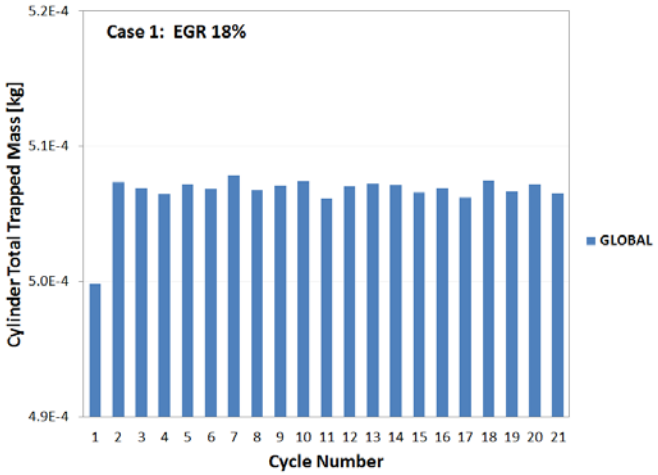

Figure 4 Cyclic trapped mass at spark timing for Case 1

Figure 5 shows the turbulent kinetic energy (TKE) at the spark timing for all 21 cycles, calculated as average quantity for the entire cylinder (results indicated with "GLOBAL") and for a spherical domain centered in the gap between the electrodes with a radius of 2.5 mm (results indicated with "SPARK"). It can be observed that global TKE features a non-negligible cyclic variability, but it is in the proximity of the spark-plug that the turbulence values show the largest fluctuations. Indeed, comparing Figure 2 to Figure 5, it can be observed that there is a correlation between the pressure peak value and the TKE value at the time of the spark in the near-spark region.

Figure 6 shows the cyclic variations of the equivalence ratio at the spark timing, in the entire cylinder as well as in the near-spark region. Although Case 1 is defined as stoichiometric operation, the global equivalence ratio is not exactly 1.0 but slightly lower (≈ 0.95). While the global equivalence ratio quickly reaches a relatively stable value, thus mirroring the trapped mass results shown in Figure 4, a large variability of the mixture composition in the proximity of the spark-plug can be observed. Some cycles (namely cycles #4, #7, #9, #13, #16, and #17) feature rich mixtures near the spark at the spark timing, while other cycles (#3, #6, #11, #18, and #20) are characterized by lean mixture in the proximity of the spark electrodes at the same time.

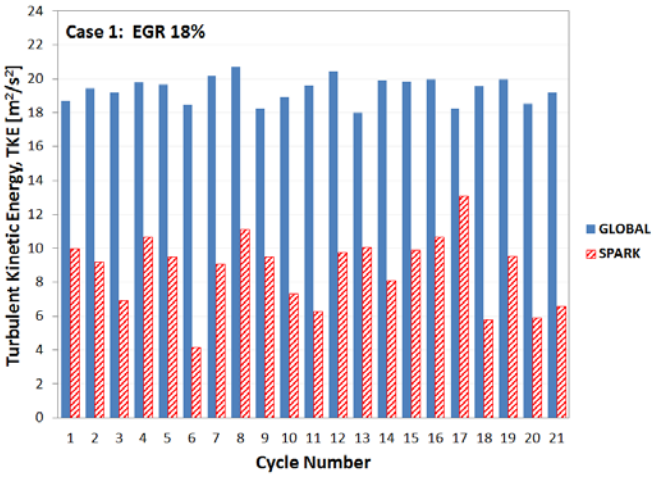

Figure 5 Cyclic TKE at spark timing for Case 1

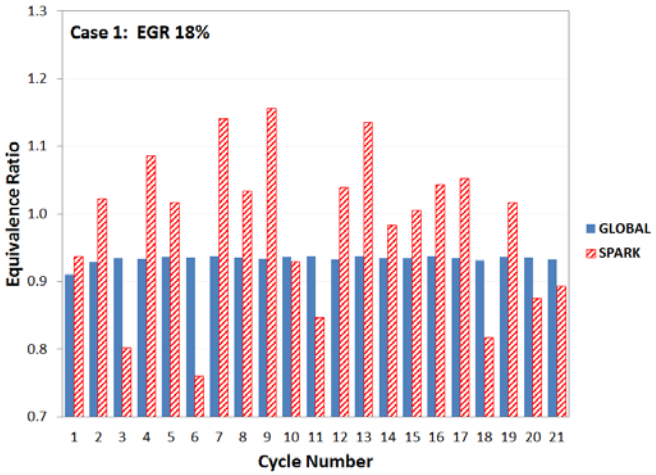

Figure 6 Cyclic equivalence ratio at spark timing for Case 1

An immediate conclusion is that the variability of the numerical pressure trace is due to the combined effect of turbulence and mixture composition that change at every cycle, with particular sensitivity to the value of these two quantities in the near-spark region. In order to understand why the effect of turbulence and mixture composition on combustion is so strong, the flame propagation mechanism is visualized for the cycles featuring the lowest and the highest peak pressure values (cycle #6 and #12 respectively). Figure 7 shows in the top row the equivalence ratio map and velocity vectors on two orthogonal planes cutting through the spark-plug, 1°CA before the spark timing, for cycle #6. It also shows the flame propagation process, described by means of the evolution of an iso-Temperature surface (at 2000 K) at four typical crank angle positions, namely 5°CA, 10°CA, 20°CA, and 30°CA after the spark timing. Figure 8 shows the same plots for cycle #12.

Cycle #6 features very slow flame propagation, which is due to relatively lean mixture and low velocity magnitude in the near-spark region. Conversely, cycle #12 shows fast combustion due to the combined effect of higher equivalence ratio and much stronger charge motion. In particular, the significant influence of the near-spark flow on early flame propagation can be observed, with the flame initially pushed away from the electrodes and quickly spreading towards the combustion chamber as a results of the strong charge motion. There is a clear difference in the flame propagation results shown in Figure 7 and Figure 8. However for these cycles both flow field and mixture stratification play the same negative or positive role and it is not straightforward to evaluate which of the two contributions is more relevant.

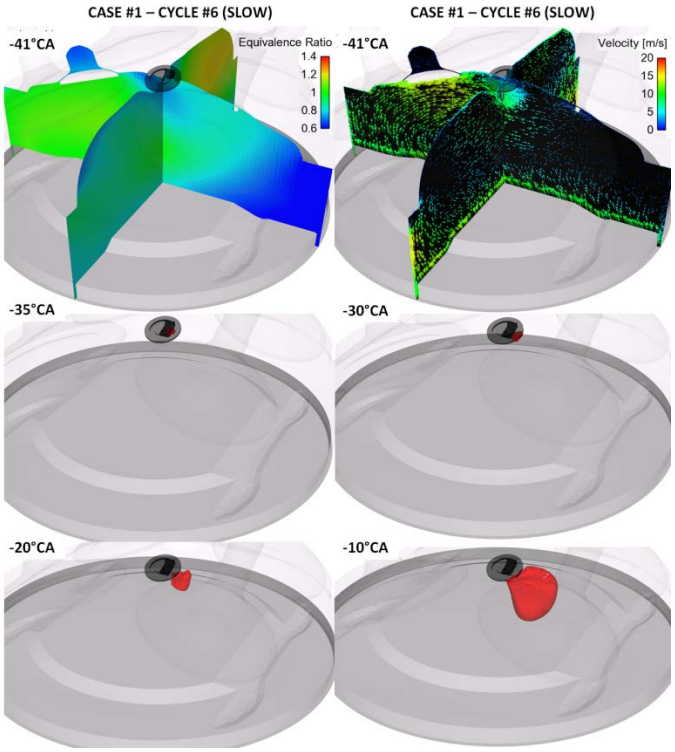

Figure 7 Effect of near-spark charge characteristics on flame propagation - Case 1 - cycle #6

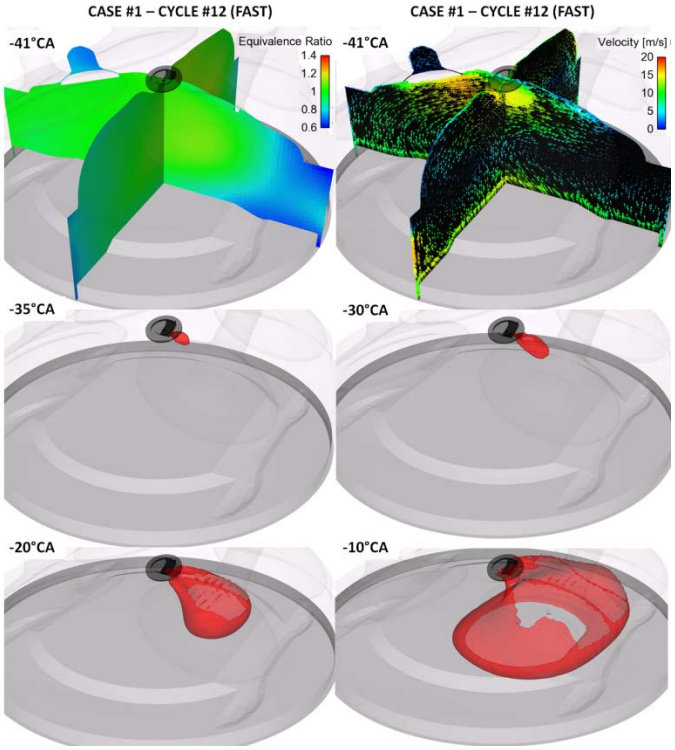

Figure 8 Effect of near-spark charge characteristics on flame propagation - Case 1 - cycle #12

Compared to cycle #12, cycle #13 shows similar near-spark TKE value (see Figure 5) but higher near-spark equivalence ratio value (see Figure 6), yet combustion is faster for the former as it can be seen in Figure 2. This is a first indicator that the equivalence ratio is not the main cause for fast or slow flame propagation and therefore not the main driver for cyclic variability. Indeed cycle #9, which features the highest value of equivalence ratio in the near-spark region, is far from being the fastest burning cycle.

Also, evaluating Figure 5 and Figure 6, cycle #17 features the highest TKE and relatively high equivalence ratio near the spark. However, the peak pressure value for cycle #17 is neither low nor high. This is because the highest TKE does not necessarily mean the strongest charge motion and therefore the TKE is maybe not the most suitable quantity to describe the effect of the flow field on flame propagation. Figure 9 shows the tumble in the entire cylinder and the flow velocity in the near-spark region at the time of the spark.

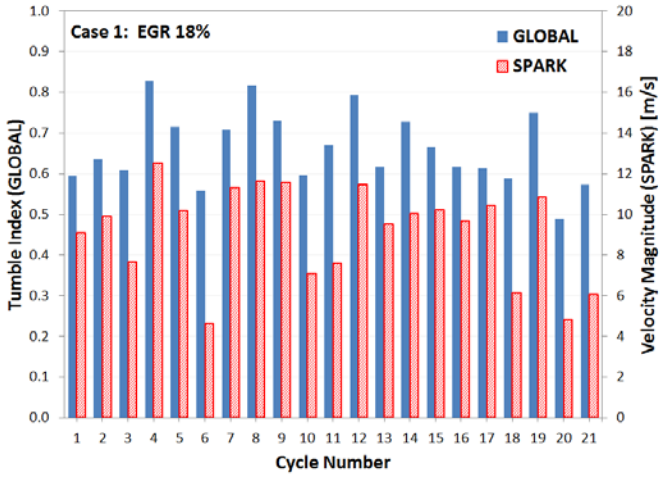

Figure 9 Cyclic tumble index (GLOBAL) and velocity magnitude (SPARK) at spark timing for Case 1

A very strong similarity of those two quantities with the pressure trace in Figure 2 can be observed. Cycles #3, #6, #18, and #20 exhibit very low peak pressure due to the combined effect of charge motion in the near-spark region and within the entire cylinder. For the same identical reason cycles #4, #12, and #19 show the highest peak values.

Section 2: Effect of the grid characteristics on the numerical results

The authors have shown that the fluctuations of the pressure traces from multi-cycle RANS are due to the variability of the flow structures, in particular in the near-spark region, which is consistent with LES studies on CCV cited in this manuscript. One of the biggest questions that could be raised is whether the cyclic variability is an effect of the computational grid changing at each time-step (and each cycle), due to the AMR algorithm used in this study, and thus a numerical artifact rather than a physical phenomenon.

To address this matter, the authors have analyzed how much the typical computational grid changes from cycle to cycle and have carried out this analysis for the case with the largest CCV, i.e. Case 1. Results shown in Figure 10 indicate that the total number of cells does not change significantly from a cycle to the next. The most significant difference in cell count when analyzing Case 1 can be detected for cycle #6 as compared to all the other cycles. As can be seen in the Figure 2, cycle #6 happens to be the lowest cycle for Case 1 featuring slow combustion. Therefore a low number of cells is expected during the first stages of combustion as an effect of the temperature AMR, while a high number of cells is expected later during combustion. Except for cycle #6, all the other cycles feature

similar mesh characteristics which is a first indicator that the large cycle-to-cycle variations observed in Case 1 do not depend on AMR.

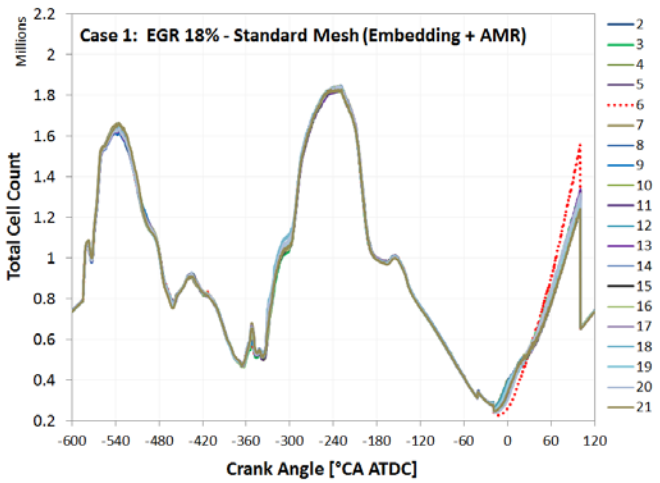

Figure 10 Crank-resolved total cell count for each simulated cycle of Case 1 (standard mesh)

An additional study performed in this paper consists of running the same simulation (Case 1) with a constant fine mesh, i.e. disabling AMR. In order to keep the minimum grid size used in the entire paper while reducing the overall cell count, the fine region includes cylinder and valves only, while the rest of the intake and exhaust domains feature a relatively coarse mesh, as summarized in Table 3 and shown in Figure 11. As AMR is disabled and only static embedding is used as refining methodology, the total cell count does not change from cycle to cycle, as can be seen in Figure 12, although the number of cells significantly increases thus requiring much longer computational times and a larger number of cores.

Table 3 Minimum grid size for Standard and Fine (NO AMR) mesh

Mesh Type	Intake	Exhaust	Cylinder	Spark
Standard Mesh	0.5 mm	0.5 mm	0.5 mm	0.125 mm
Fine Mesh (NO AMR)	4 mm	4 mm	0.5 mm	0.125 mm

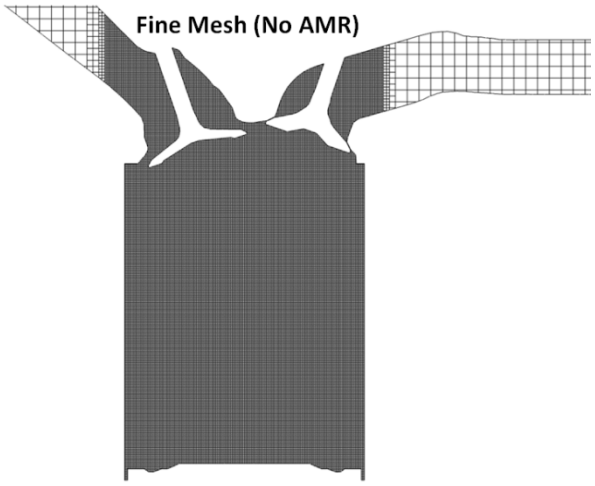

Figure 11 Constant fine mesh used to remove the effect of AMR on CCV

Due to longer computational time, the multi-cycle simulation test with static fine mesh was performed for eight cycles only. However the numerical results already indicate that, even when a static computational grid is used, large fluctuations in the numerical pressure trace are to be expected, as can be seen in Figure 13. It is worth highlighting that while the CCV are still quite large with a static mesh, the peak pressure values are relatively low as compared to the results using a standard mesh.

The reason for CCV again lies in the cyclic variability of the flow structures. Indeed, there is a strong similarity between the global (tumble) and local (velocity magnitude around the spark) flow field properties shown in Figure 14 and the numerical pressure traces shown in Figure 13. Also, it can be seen that tumble and velocity values are significantly lower than the same values using a standard mesh (see Figure 9 as a reference). Hence, while cyclic variability does not depend on AMR, having a coarse mesh where the flow is generated (intake and exhaust ports) leads to a miscalculation of the flow properties that affects the numerical predictions in terms of flame propagation and in-cylinder pressure. Conversely, AMR allows resolving the velocity gradients everywhere (including the ports) without significantly increasing the computational time and it is an effective approach to deliver high accuracy within reasonable computational time.

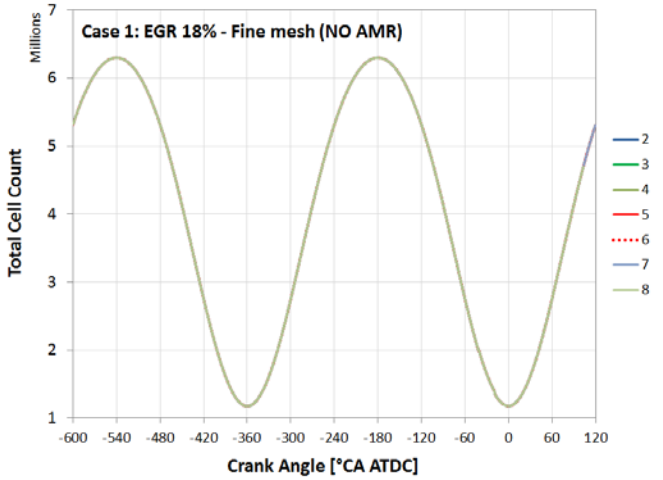

Figure 12 Crank-resolved total cell count for each simulated cycle of Case 1 (static fine mesh)

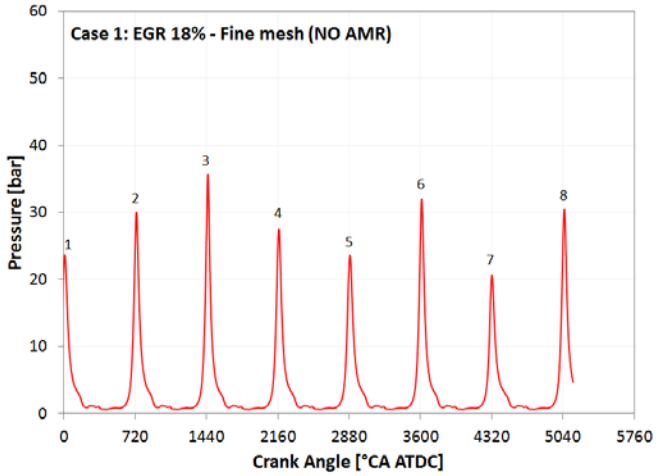

Figure 13 Numerical pressure traces for Case 1 (static fine mesh)

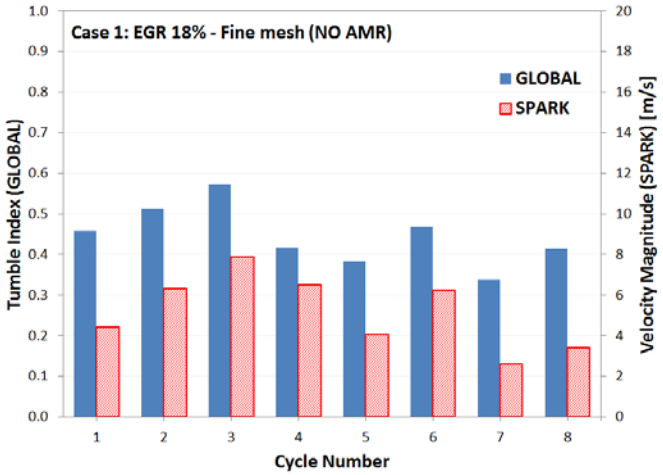

Figure 14 Cyclic tumble index (GLOBAL) and velocity magnitude (SPARK) at spark timing for Case 1 (static mesh)

Section 3: Cold-flow analysis and CCV

To address concerns regarding the effect of combustion on CCV, the impact of re-initialization at EVO on the cyclic fluctuations of the equivalence ratio, or the perturbation introduced by restarting the simulation, the analysis of the evolution of the cold flow is carried out for 10 consecutive cycles by suppressing the combustion event. Figure 15 shows the results of the cold-flow analysis for Case 1 in terms of total cell count. It can be seen that the cyclic variability of the number of cells is greatly reduced compared to a fired case (see Figure 10 as a reference) and no significant differences can be detected after the second simulation cycle. Also, as shown in Figure 16 the numerical pressure traces quickly converge and no differences can be detected between the cycles after the second cycle, while the first cycle is still slightly affected by the initial conditions.

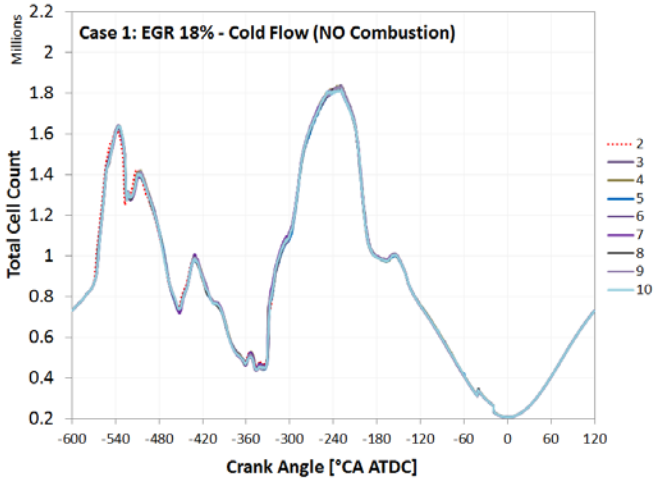

Figure 15 Crank-resolved total cell count for each simulated cycle of Case 1 suppressing combustion (cold-flow analysis)

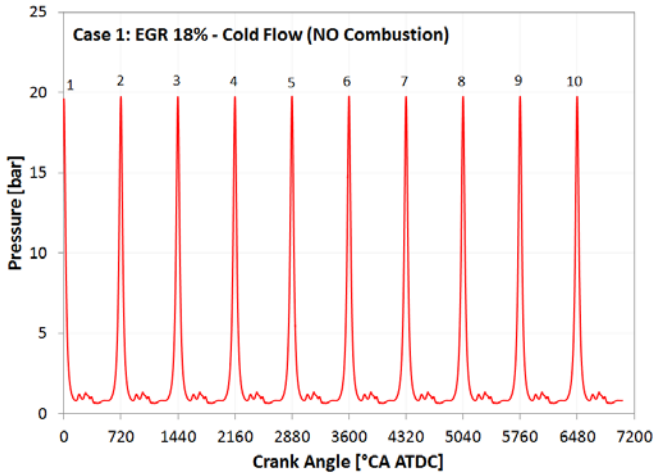

Figure 16 Numerical pressure traces for Case 1 suppressing combustion (cold-flow analysis)

However, while cell count and in-cylinder pressure do not suffer from significant cyclic variability, non-negligible fluctuations in the flow characteristics persist as can be seen in Figure 17. While suppressing combustion significantly reduces the flow intensity and the cyclic variability, there is no clear convergence pattern of global and near-spark flow characteristics. Therefore, the cyclic variability of the in-cylinder flow is an intrinsic property of internal combustion engines and can be shown by using RANS even for a non-fired case. If combustion is re-activated, the slight changes in the flow configuration from cycle-to-cycle observed in Figure 17 would certainly lead to changes in flame propagation and combustion progress, thus delivering larger pressure fluctuations discussed earlier for Case 1.

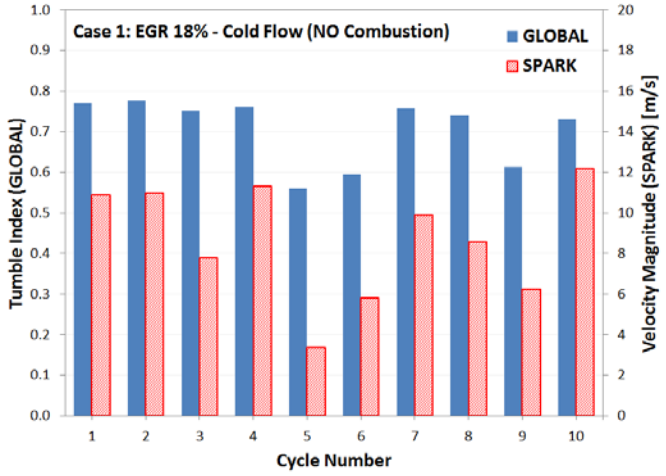

Figure 17 Cyclic tumble index (GLOBAL) and velocity magnitude (SPARK) at spark timing for Case 1 suppressing combustion (cold-flow analysis)

Section 4: Analysis of multi-cycle RANS results for stoichiometric combustion

The magnitude of CCV should be strongly correlated to the stability of the examined operating condition. Indeed, when multi-cycle RANS is carried out for a relatively stable operating condition, for example Case 2 (EGR = 0%), the numerical cyclic variability with RANS is significantly reduced, as shown in Figure 18, although it is not entirely eliminated. Even though the numerical pressure traces are

similar to the average experimental pressure trace and a more stable pressure trace in general can be seen (see Figure 19), again there is no converging trend.

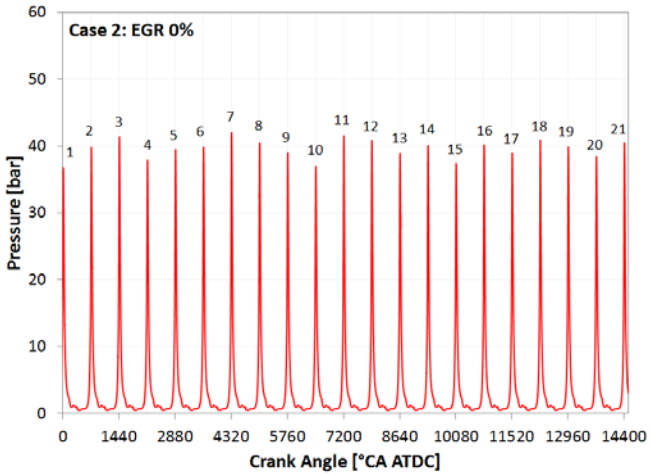

Figure 18 Numerical pressure traces for Case 2

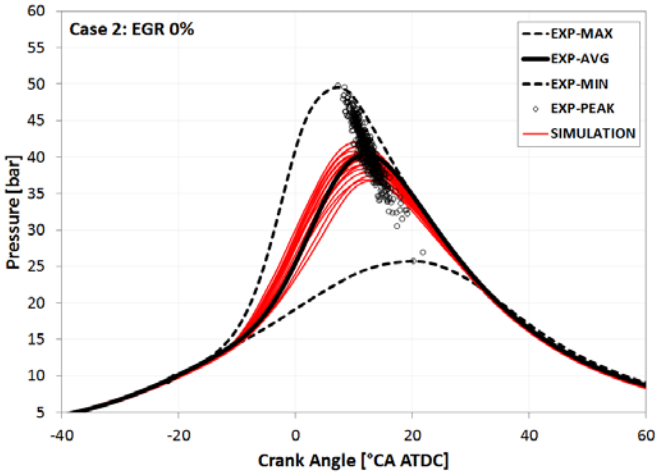

Figure 19 Comparison between numerical and experimental pressure traces for Case 2 (21 simulated cycles vs. 500 experimental cycles)

Many of the engine parameters analyzed in the first section of these results (Case 1) are not shown here since the results for Case 2 show similar trends, although with smaller cyclic fluctuations. Figure 20 shows the cyclic variability of the in-cylinder tumble and near-spark velocity magnitude at spark timing. In general, lower tumble values for Case 2 as compared to Case 1 are observed, due to lower intake pressure values for the non-dilute case to ensure the same load as the EGR-dilute case. Also, the spark event occurs later in the compression stroke for Case 2, which leads to a further reduction in the magnitude of tumble. Nevertheless, lower tumble does not necessarily mean lower velocity magnitudes in the near spark region. Actually, the magnitude of velocity vectors at spark timing for the stoichiometric case is higher than for EGR-dilute operation as can be seen comparing Figure 20 to Figure 9.

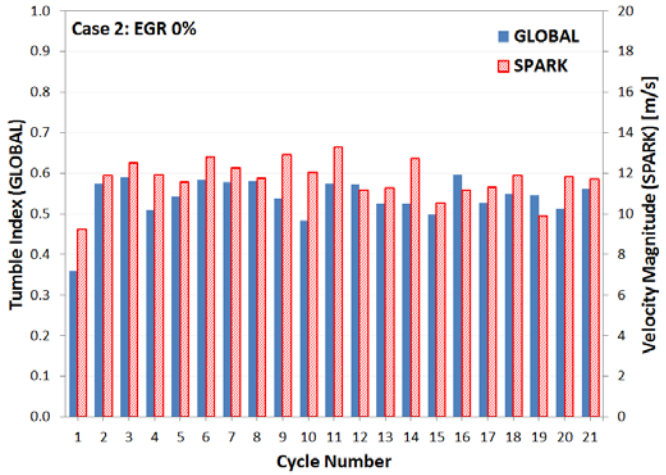

Figure 20 Cyclic tumble index (GLOBAL) and velocity magnitude (SPARK) at spark timing for Case 2

Even though the cyclic fluctuations of the charge motion for Case 2 are lower than for Case 1, there are still significant differences between the cycles that cannot be observed in the pressure traces. Figure 21 and Figure 22 show the effect of the charge conditions on flame propagation for Case 2, cycles #10 and #11, i.e. the cycles characterized by the lowest and highest peak pressure respectively.

While the flow fields show some differences, especially in the near-spark region, the effect on flame propagation is limited. It can be clearly seen that for Case 2 the combustion process is more consistent from a low cycle to a high cycle and the cause is the combination of smaller cyclic fluctuations of the in-cylinder flow and smaller effect of the flow itself on flame propagation. Indeed, if Figure 21 and Figure 22 are compared to Figure 7 and Figure 8 respectively, it can be noticed that the flame propagation is much faster for Case 2 as compared to Case 1.

The main reason for reduced CCV is the change of the operating condition. Case 2 is characterized by stoichiometric non-dilute mixtures ignited at higher temperature (SA = -24°CA ATDC) while Case 1 is characterized by highly EGR-dilute mixtures ignited at lower temperature (SA = -40°CA ATDC). As a result, the flame propagation is faster for Case 2 and the fact that the in-cylinder flow does not greatly affect flame propagation is an indicator that the combustion process for Case 2 is much more stable than for Case 1.

When the role of charge motion on early flame propagation becomes less important, as for relatively stable cases, RANS can capture only small cyclic variations. The larger cyclic variability for cases characterized by low COV_{IMEP} with LES [5,8] likely comes from larger cyclic flow variability as an effect of more accurate characterization of the in-cylinder flow.

To confirm this hypothesis, a cold-flow analysis is performed for Case 2 as well. The results in Figure 23 show cyclic variability of tumble and near-spark velocity that are consistent with the cyclic variability of the flow for Case 1 (Figure 17). This suggests that the variability of the flow is very similar identical in the two cases, while the effect on flame propagation and combustion is different. It is also worth noting that the slight differences between Figure 17 and Figure 23 are due to the different spark timing for Case 1 and Case 2 respectively. Similar differences can be notice between Figure 9 (Case 1 with combustion) and Figure 20 (Case 2 with combustion).

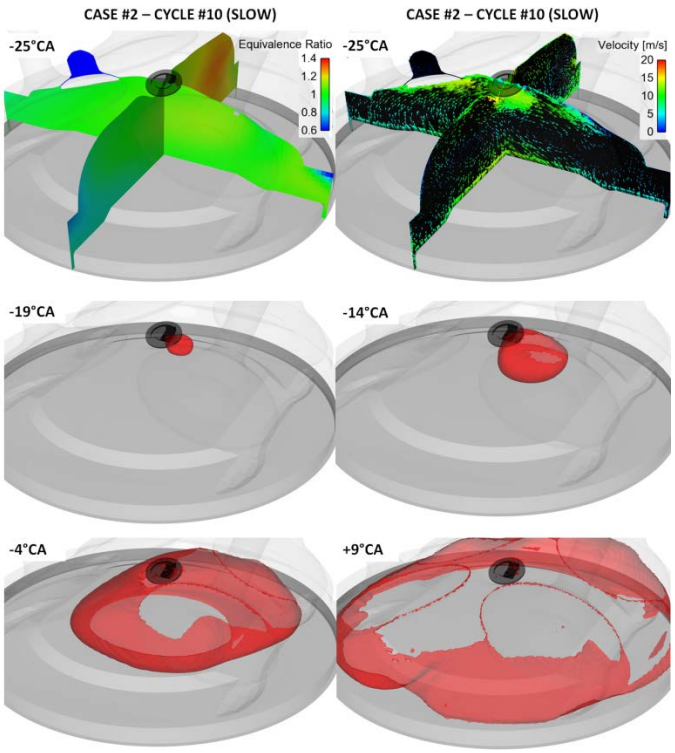

Figure 21 Effect of near-spark charge characteristics on flame propagation - Case 2 - cycle #10

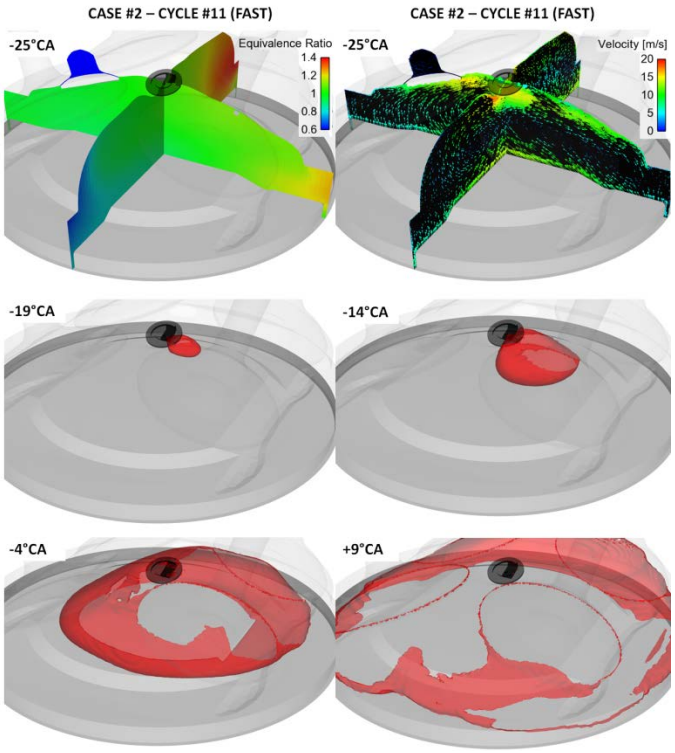

Figure 22 Effect of near-spark charge characteristics on flame propagation - Case 2 - cycle #11

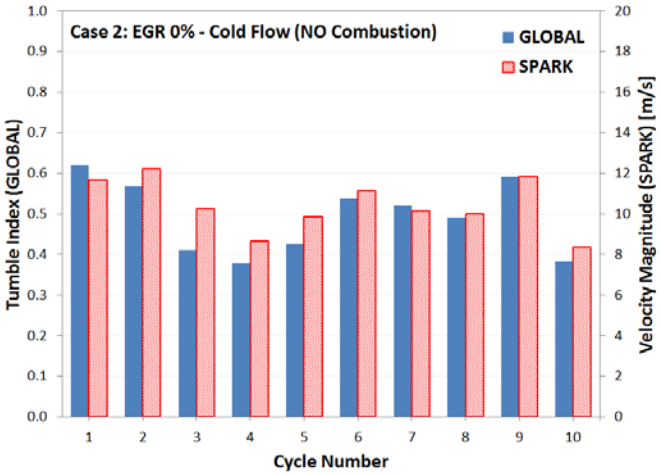

Figure 23 Cyclic tumble index (GLOBAL) and velocity magnitude (SPARK) at spark timing for Case 2 suppressing combustion (cold-flow analysis)

Section 5: Effect of numerical viscosity on CCV

The numerical results shown in this paper demonstrate that RANS is capable of calculating the flow variability to some extent. While LES are expected to deliver a more accurate characterization of the flow scales and introduce the stochastic component of the flow, multi-cycle RANS should not always be expected to deliver converging pressure traces, and in some cases (such as Case 1 of this paper) can capture large CCV.

A common reason why RANS is erroneously expected to suppress cyclic variability and deliver a converging "average" result is the high numerical viscosity that characterizes many RANS simulations. To clarify and validate this statement, the analysis of the cold-flow is carried out for Case 1 while progressively increasing numerical viscosity by modifying specific numerical settings such as grid resolution and order of numerics. 10 consecutive cycles for Case 1 (suppressing combustion) are simulated using:

- The standard mesh used throughout this paper and defined in the CFD Methodology chapter, here referred to as "Fine-AMR"
- A similar mesh (same level of embedding and AMR) with bigger base grid (8 mm), here referred to as "Coarse-AMR"
- A coarser mesh with 8 mm base grid and embedding but suppressing AMR, here referred to as "UltraCoarse-NO-AMR"
- The standard mesh used throughout this paper while switching the numeric from central (2^{nd}) to upwind (1^{st}), here referred to as "Fine-AMR-Upwind"

Figure 24 shows the crank-resolved tumble for 10 consecutive cycles for the 4 cases tested. It should be mentioned that upwind schemes are very dissipative and using 1^{st} order is similar in effect to increasing the cell size. More importantly, both coarse mesh and low order of numeric increase numerical viscosity.

The results show that switching from fine mesh (red curve) to coarse (blue) and ultra-coarse (green) mesh results in the tumble being progressively under-estimated. The numerical results for a first order upwind scheme (black curve) are very similar to those from the ultra-coarse mesh, which demonstrates that upwinding schemes are very dissipative. Not only coarse mesh and upwinding scheme both reduce the calculated tumble - which consequently would have a weaker

effect on flame propagation and CCV – but the cyclic variability of the calculated tumble is strongly suppressed, as can be observed in detail in Figure 25. If these simulations include combustion, the cyclic variability would be largely reduced and RANS results would deliver the "more conventional", although less accurate, converging results.

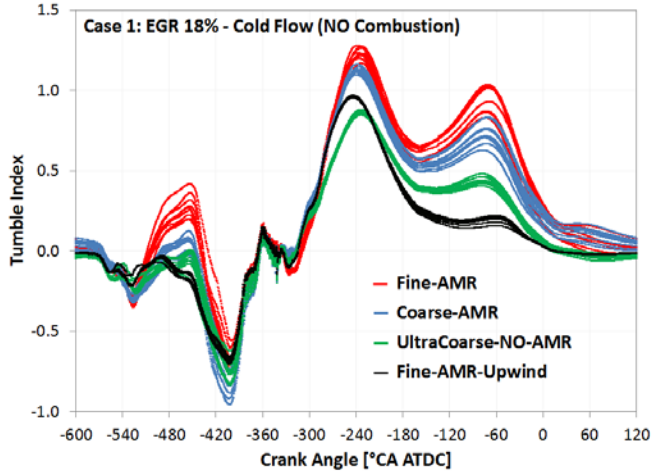

Figure 24 Crank-resolved tumble for 10 simulated cycles of Case 1 suppressing combustion (cold-flow analysis) and using several mesh strategies

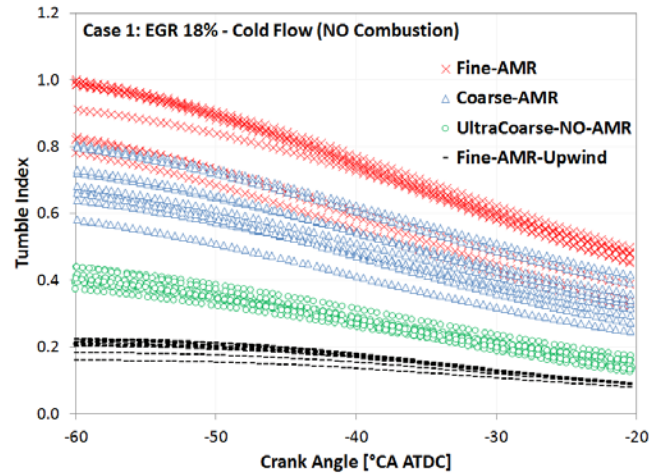

Figure 25 Tumble index prior to spark timing for 10 simulated cycles of Case 1 suppressing combustion (cold-flow analysis) and using several mesh strategies

Previous work [13] showed how a coarse mesh or an enforced 1st order numerical scheme may significantly reduce the cyclic variability even for highly dilute combustion. A typical multi-cycle RANS result obtained for Case 1 with coarse mesh and upwind scheme is shown in Figure 26 [13]. Coarse mesh would deliver very low pressure cycles due to two main reasons: 1) the flow magnitude is under-estimated, and 2) the SAGE model does not work well with coarse meshes, due to large sub-grid effects [21]. If the same simulation is executed with the standard fine mesh but forcing a 1st order of discretization, again a converging solution can be detected after the 3rd cycle. In both cases the solution is repeatable – due to the repeatability of the flow field – but inaccurate. In both cases, coarse mesh and 1st order numerics, numerical viscosity significantly increases. Hence, numerical viscosity increases the repeatability of the numerical results but also reduces accuracy.

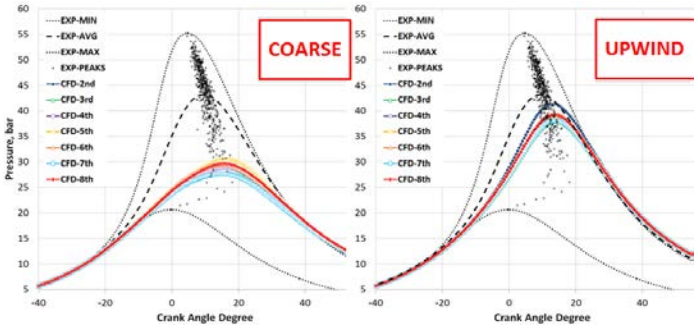

Figure 26 Typical multi-cycle RANS results using coarse mesh (left) or up-winding scheme (right) [13]

Overall, if numerical viscosity is properly reduced, RANS is capable of capturing some CCV features in multi-cycle engine simulations and can clearly distinguish cases with high and low combustion stability. While for less stable cases the numerical results feature large variability, the latter is significantly reduced when simulating more stable operating conditions.

To reinforce the statements made above about numerical viscosity and face such a conceptual matter on a much more simple geometry, the unsteady RANS results of a cylinder in cross flow are here briefly illustrated. These results were recently published using the same CFD code and similar settings (embedding and AMR) to the ones described in this manuscript. Details about the simulation setup can be found in literature [14], while Table 4 describes only the relevant numerical settings used for the three different simulations performed.

Table 4 Simulation parameters for cylinder in cross flow [14]

Case	CYL 1	CYL 2	CYL 3
Scheme	1st upwind	2nd central	1st upwind
Base grid size	10 mm	10 mm	0.2 mm
Min grid size	1.25 mm	1.25 mm	0.025 mm

Figure 27 shows the resulting vorticity field for each of the three cases that were simulated. The simulations were run long enough to reach a pseudo steady-state. For CYL 1, the solution does reach a true steady flow, whereas both CYL 2 and CYL 3 reach a cyclic solution with vortices shedding behind the cylinder.

To understand these results, it is helpful to estimate the effective viscosity of these flows. There are three contributors to the effective viscosity of the flow: molecular viscosity, numerical viscosity, and turbulence viscosity. For all the simulated cases, the molecular viscosity (that of air) was small enough to essentially be irrelevant since a RANS turbulence model was being used. The turbulent viscosity varies spatially, as can be seen in Figure 28. However, for rough estimation purposes the turbulent viscosity will be considered to be $5.0e^{-4}$ m^2/s for all three cases, as only minor differences can be observed between the three cases. The numerical viscosity is different for each case. For first order numerics, the numerical viscosity can be roughly estimated as u*dx/2 (this is a very rough estimate, but should be sufficient for our purposes). Using this estimate (based on the smallest dx in the domain), CYL 1 has a numerical viscosity of around $3.1e^{-2}$ m^2/s and CYL 3 has a numerical viscosity of around $6.2e^{-4}$ m^2/s. Using these estimates for numerical and turbulent viscosity, the effective Reynolds number is about 20 for CYL 1, 1200 for CYL 2, and 540 for CYL 3.

As expected for these Reynolds numbers, CYL 1 does not shed vortices but both CYL 2 and CYL 3 do exhibit vortex shedding. The frequency of the shedding vortices for both CYL 2 and CYL 3 is about 1100 s^{-1}, which corresponds to a Strouhal number of 0.22. This correlates well with the expected Strouhal number of about 0.2 for Reynolds numbers in this range. The most relevant outcome of this study is that CYL 2 and CYL 3, which have less numerical diffusion than CYL 1, result in an unsteady solution, i.e., they do not give an ensemble averaged flow-field, even when using a RANS turbulence model. The turbulent viscosity does act to destroy the smaller scales, but it also allows larger scales to exist, even if they are time-varying.

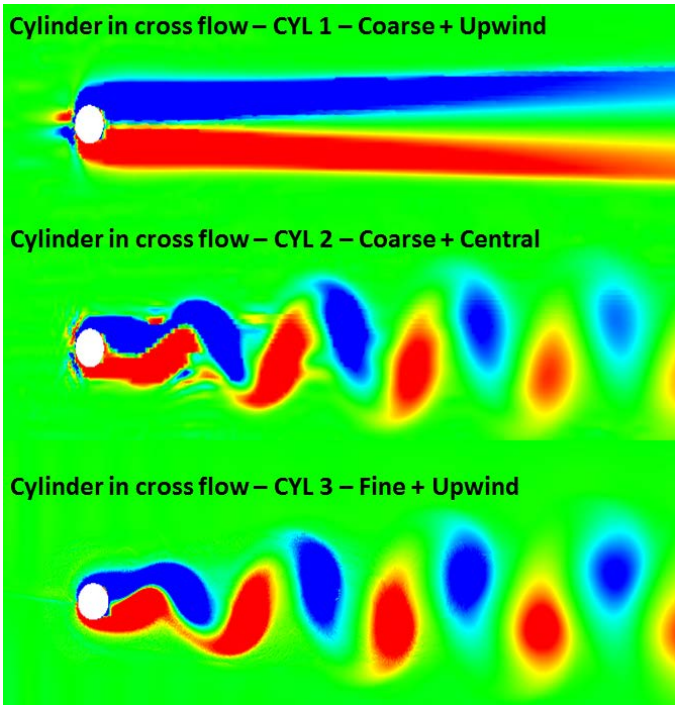

Figure 27 Images of vorticity for the cylinder in cross flow simulation [14]

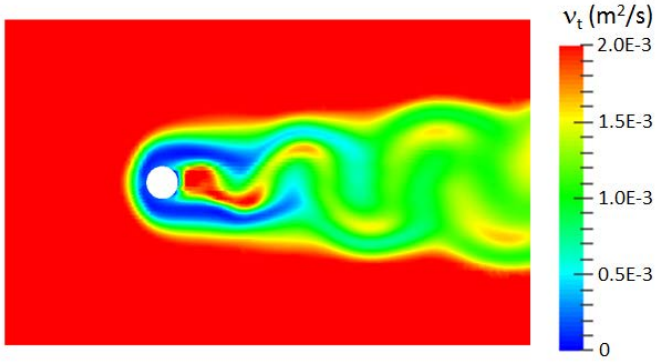

Figure 28 Turbulent viscosity distribution for the cylinder in cross flow simulation

Similar analysis can be carried out on the cold-flow simulations shown at the beginning of this section. Here the main issue is that turbulent viscosity significantly changes during the cycle and furthermore it is not easy to provide a rough estimate of numerical viscosity for a second order discretization, which is the most used scheme in the engine calculations shown in this paper.

Figure 29 shows the average turbulent viscosity in the cylinder region for three consecutive cycles (from cycle #1 to cycle #4) for three of the four cases shown in Figure 24, namely "Fine AMR", "Ultra-Coarse-NO-AMR", and "Fine-AMR-Upwind". It can be seen that turbulent viscosity is progressively decreased consistently with the tumble index shown in Figure 24, but maintains the same order of magnitude even in the cases with the highest numerical viscosity (ultra-coarse mesh or upwind scheme).

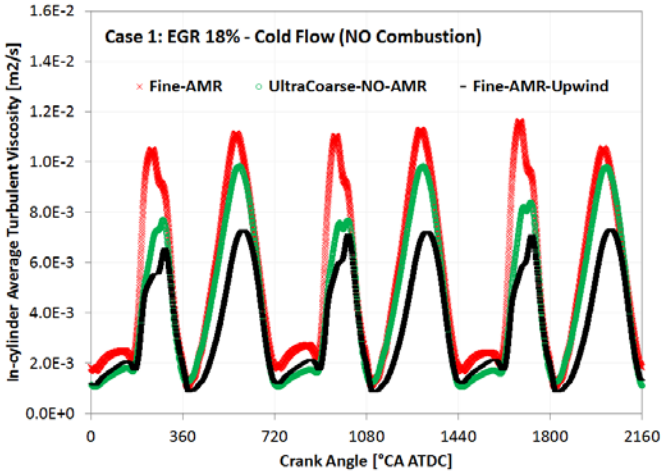

Figure 29 Cylinder average turbulent viscosity for engine cold flow simulations from cycle #1 to cycle #3

Since this is just an average value over the entire cylinder domain, Figure 30 shows the distribution of turbulent viscosity in the central tumble plane at +620°CA ATDC, i.e. during compression stroke and right after IVC, for the two fine cases employing central and upwind scheme. These two cases feature the highest and lowest turbulent viscosity value respectively. Despite the spatial variability, turbulent viscosity in the bulk flow will be considered to be 1.0-1.5e^{-2} m^2/s for both cases. The velocity magnitude in the same plane at the same crank angle, not reported here for the sake of brevity, ranges from 0 m/s to 14 m/s, and it is approximately 7 m/s in the bulk flow. Mesh size is 0.5-1.0 mm. These quantities deliver a value for numerical viscosity of u*dx/2 = 1.75-3.5 e^{-3} m^2/s, i.e. about 5-10 times lower than turbulent viscosity.

It is worth noting that for the central scheme case (Fine-AMR) turbulent viscosity is slightly higher, while numerical viscosity might be significantly lower, thus further increasing the ratio between turbulent and numerical viscosity.

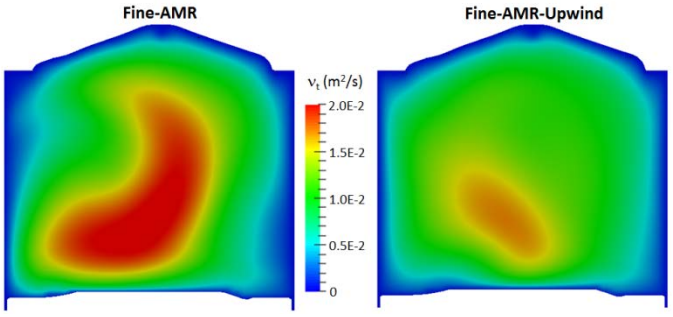

Figure 30 Turbulent viscosity distribution for engine cold flow simulations at +620°CA ATDC

However, both the turbulent and numerical viscosity values change significantly during the same engine cycle. In this paper it is shown that cyclic variability is mostly due to the in-cylinder flow, which is generated during the gas exchange phase. Figure 31 shows turbulent viscosity and velocity magnitude distributions on a vertical plane through the intake and exhaust valves at +460°CA ATDC, i.e. at maximum intake valve lift, for the Fine-AMR-Upwind case. Turbulent viscosity is of the order of $1.0e^{-3}$ m^2/s, while velocity is approximately 25 m/s in the bulk flow. Mesh size is still 0.5-1.0 mm, which delivers a rough estimate of $0.625\text{-}1.25e^{-2}$ m^2/s for the numerical viscosity. Also, velocity is even higher (≈ 50-100 m/s) and turbulent viscosity is even lower (≈ $1.0\text{-}5.0e^{-4}$) in the intake ports, which is where the in-cylinder flow is generated. Therefore, for this case numerical viscosity is quite larger than turbulent viscosity, consistently with case CYL 1 shown above. When switching to higher order of numerics (Fine-AMR), turbulent viscosity will only be slightly increased (about twice as much) but numerical viscosity might be significantly reduced (one or two orders of magnitude), and this will reduce the effect of numerical viscosity in damping cyclic variability.

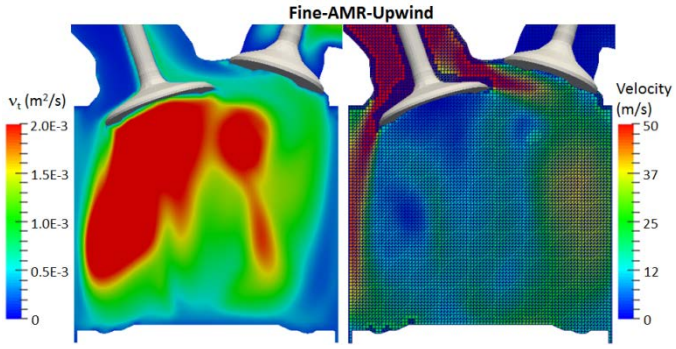

Figure 31 Turbulent viscosity and velocity distributions for the Fine-AMR-Upwind cold flow simulation at +460°CA ATDC

Section 6: The effect of mesh resolution on CCV prediction using flamelet combustion modeling

The G-Equation model is based on the assumption that the premixed turbulent combustion is in either the corrugated flamelet or the thin reaction zone regime. With these assumptions, the turbulent flame front can be tracked by solving for the mean and variance of a non-reacting scalar, G [25]:

$$\frac{\partial \rho \tilde{G}}{\partial t} + \frac{\partial \rho \tilde{u}_i \tilde{G}}{\partial x_i} = -D_t' k \left|\frac{\partial \tilde{G}}{\partial x_i}\right| + \rho_u s_t \left|\frac{\partial \tilde{G}}{\partial x_i}\right|$$

$$\frac{\partial \rho \widetilde{G''^2}}{\partial t} + \frac{\partial \rho \tilde{u}_i \widetilde{G''^2}}{\partial x_i} = \frac{\partial}{\partial x_i}\left(\rho D_t \frac{\partial \widetilde{G''^2}}{\partial x_i}\right) + 2\rho D_t \frac{\partial \tilde{G}}{\partial x_i}\frac{\partial \tilde{G}}{\partial x_i} - c_s \rho \widetilde{G''^2}\frac{\varepsilon}{k}$$

Where s_t is the turbulent flame speed, ρ_u is the unburned density, k is the turbulent kinetic energy, ε is the turbulent dissipation, and c_s is a user-supplied constant. In the approach followed in this paper, the variance of G is not solved, therefore the turbulent diffusion, D_t, is given by:

$$D_t = \frac{c_\mu}{Sc}\frac{k^2}{\varepsilon}$$

The laminar flame speed is calculated by using the Gulder correlation [26], while the following turbulent burning velocity relationship, proposed by Peters [24], is used for calculating the turbulent flame speed:

$$s_t = s_l + u'\left\{-\frac{a_4 b_3^2}{2b_1}Da + \left[\left(\frac{a_4 b_3^2}{2b_1}Da\right)^2 + a_4 b_3^2 Da\right]^{1/2}\right\}$$

where u' is the root mean square of the turbulent fluctuating velocity, s_l is the laminar flame speed, Da is the Damkohler number, and a_4, b_1, and b_3 are modeling constants. The recommended value for b_1 is 2.0. However, in this paper b_1 is tuned to match the experimental data. In fact, as the grid resolution increases the turbulence levels also increase in the domain and therefore this constant needs to be adjusted. A larger value of b_1 increases the turbulent flame speed while a smaller value decreases the turbulent flame speed.

Table 5 shows the numerical settings (mesh size and order accuracy) used to simulate Case 1 (EGR 18%) using the G-equation model. GEQ1 basically replaces the SAGE model with G-equation without changing the other settings. GEQ2 uses a coarser mesh and lower order than GEQ1.

Table 5 Numerical settings for G-equation combustion cases

Case	GEQ1	GEQ2
Scheme	2nd central	1st upwind
AMR level	3	3
Embedding level	Up to 5	Up to 5
Base grid size (mm)	4	8
Refined grid size (mm)	0.125 (spark) 0.5 (flame) 0.5 (gas-exchange)	0.25 (spark) 1.0 (flame) 1.0 (gas-exchange)
b_1 constant (G-equation)	1.85	3.25

Figure 32 shows the comparison between numerical and experimental data for Case 1 using the G-equation model (GEQ1). In order to match the average experimental pressure in a qualitative way, b_1 was slightly reduced to 1.85 instead of the recommended 2.0 value.

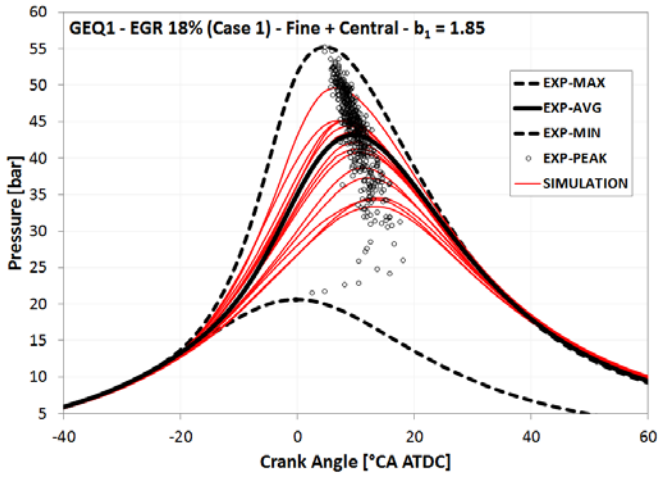

Figure 32 Comparison between numerical and experimental pressure traces for Case 1 using the G-equation model – GEQ1

The main conclusion from Figure 32 is that CCV with RANS occur regardless from the specific approach used to model combustion. The cause for this behavior is again the variability of the flow properties, as can be seen in Figure 33. The authors would like to point out that

the degrees of cyclic variability of tumble and near-spark velocity shown in Figure 33 and Figure 9 are almost identical.

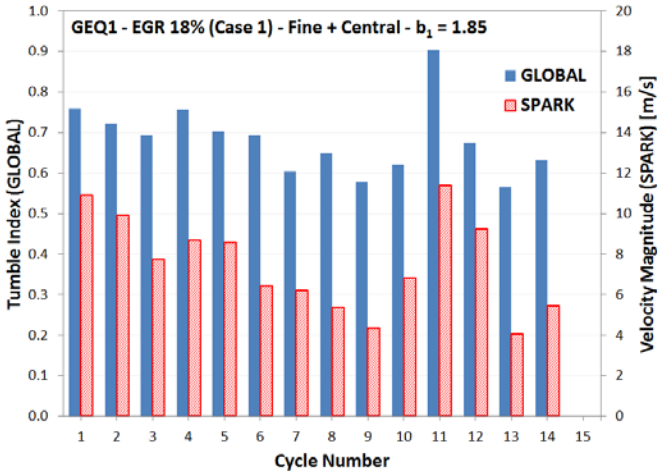

Figure 33 Cyclic tumble index (GLOBAL) and velocity magnitude (SPARK) at spark timing for Case 1 using the G-equation model – GEQ1

When the same case is simulated using coarser mesh and lower order of accuracy (GEQ2), CCV are greatly reduced as can be seen in Figure 34.

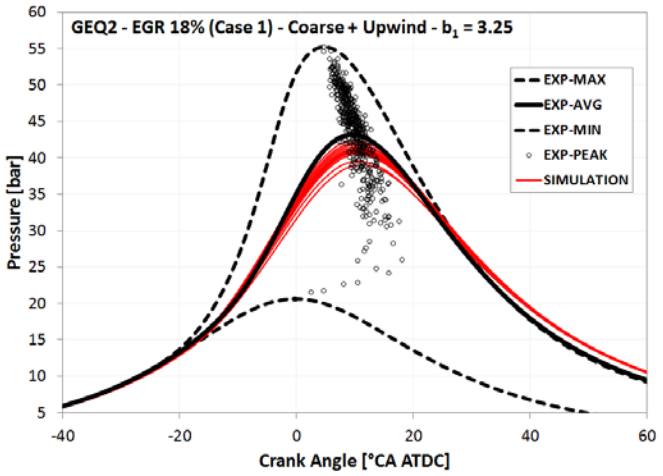

Figure 34 Comparison between numerical and experimental pressure traces for Case 1 using the G-equation model – GEQ2

Figure 35 shows the variability of the flow properties for the GEQ2 case. What immediately stands out is that not only the degree of variability of tumble ratios and velocity magnitudes is small, but those values themselves are extremely low. These results are consistent with the tumble ratios profile shown in Figure 24 and Figure 25, i.e. high numerical viscosity significantly reduces both flow intensity and variability. Indeed, to match the experimental data, the b_1 constant was significantly increased ($b_1 = 3.25$) to overcome the reduction of the turbulent flame speed due to the low intensity of the cylinder flow. However, while more repeatable, the numerical solution is less accurate, as partially shown by the over-prediction of the in-cylinder pressure during the power stroke.

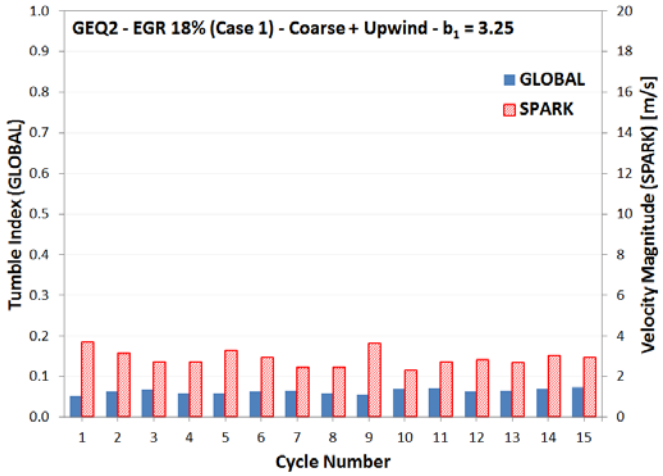

Figure 35 Cyclic tumble index (GLOBAL) and velocity magnitude (SPARK) at spark timing for Case 1 using the G-equation model – GEQ2

Section 7: Using multi-cycle RANS to qualitatively predict combustion stability

Recent work analyzed the effect of ignition properties on numerical and experimental cyclic variability for EGR dilute as well as non-dilute combustion [27]. Cases 1 and 2 were simulated for the same number (21) of consecutive cycles by also using a higher energy multi-pulse ignition profile. These cases are here referred as to Case 1b and 2b respectively, to distinguish them from Case 1a and 2a (using standard single-pulse ignition). Table 6 highlights the main differences between the four cases, while all other parameters that are not reported in Table 6 are identical. Looking at the COV_{IMEP} experimental values, it should be noted that using a multi-pulse higher energy ignition profile has a beneficial effect on dilute combustion (cases 1a and 1b) and no effect on non-dilute combustion (cases 2a and 2b).

Table 6 Additional specifications of the examined test cases [27]

Test Case	1a	1b	2a	2b
EGR [%]	18	18	0	0
Ignition Energy [mJ]	75	150	75	150
Number of Pulses	1	5	1	5
Ignition Duration [ms]	0.5	1.2	0.5	1.2
COV_{IMEP} [%] measured over 500 cycles	8	4	1.5	1.5
COV_{CA-50} [%] measured over 500 cycles	13	11	9	9

Figure 36 shows the comparison between numerical and experimental results in terms of COV_{CA-50}, where CA-50 is here defined as the crank angle of 50% MFB. Numerical results are shown as cumulative numbers on 20 cycles (the first cycle is discarded). The dash lines represent the experimental average values of COV_{CA-50}. As can be seen, RANS under-predicts cyclic variability for the non-dilute cases (2a and 2b) while it does a much better job for the dilute cases (1a and 1b). More importantly, the trend and the order of magnitude of COV_{CA-50} are both well predicted by RANS simulations. Therefore, it can be stated that RANS can qualitatively describe typical combustion stability features.

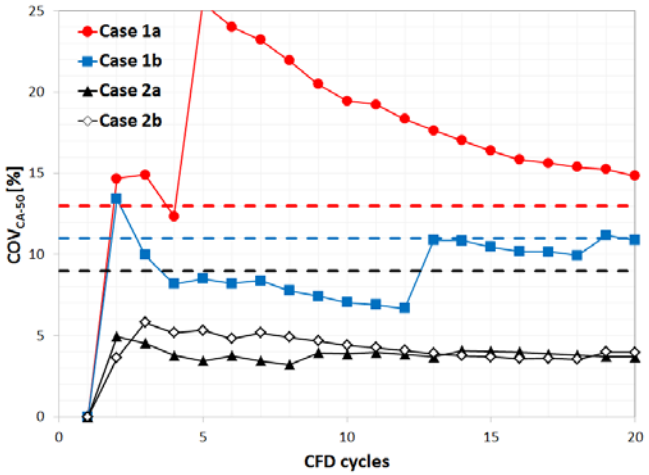

Figure 36 Comparison between numerical and experimental COVCA-50 for Cases 1a, 1b, 2a, 2b [27]

Similar conclusions can be drawn by looking at Figure 37 , showing the flame development angle (CA0-10, also widely referred as to ignition delay) and the combustion duration (CA10-90) for all the cases simulated in this paper. All 20 simulated cycles (the first cycle is discarded) are shown to highlight the effect of the ignition properties on combustion stability. As can be seen, stoichiometric operation does not show much variability as compared to dilute operation, regardless from the specific ignition profile that is used. In general, while the flow variability is similar in the two cases (as shown in Figure 17 and Figure 23), stoichiometric conditions feature faster combustion due to the reduced amount of residuals and generally later ignition timing (which leads to higher temperature and pressure values in the cylinder at the time of the spark). As a consequence, the flame speed increases and the combustion duration becomes insensitive to the flame development angle.

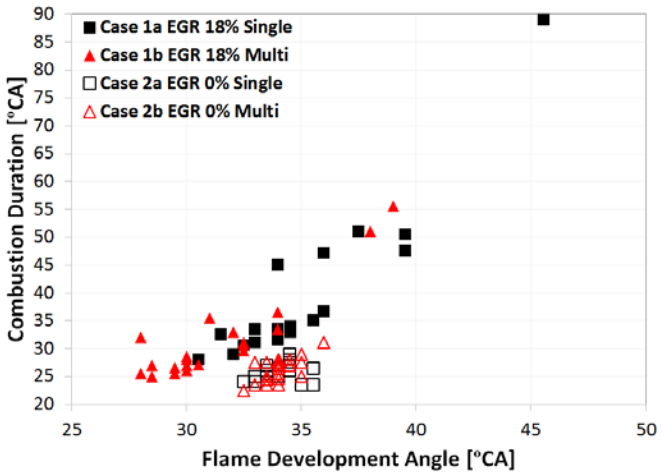

Figure 37 Effect of ignition characteristics on combustion stability for stoichiometric and dilute operations, CFD results [27]

Under dilute operation, the flame development angle gains more importance as a slow flame development negatively affects the entire flame propagation and combustion duration. The effect of the in-cylinder flow gains more importance as well, in that the large cyclic variations observed in Figure 3 are due to the variability of the flow from a cycle to the next. In particular, the flow has a significant effect on the early flame propagation, thus affecting the flame development angle. Dilute operation also shows an increased importance of the ignition characteristics on the combustion event. A multi-pulse ignition profile is capable of reducing the flame development angle. This leads to shorter combustion duration and allows avoiding poor combustion and misfires.

As can be seen in Figure 38, numerical results closely mimic the experimental dataset in terms of combustion metrics. Only slight differences can be noticed that might come from multiple sources of inaccuracies, such as equivalence ratio and heat transfer calculations. Nevertheless, even keeping those inaccuracies into account, the proposed methodology shows the potential to capture and analyze the impact of advanced ignition sources on cyclic variability, both for conventional and advanced (dilute) SI combustion.

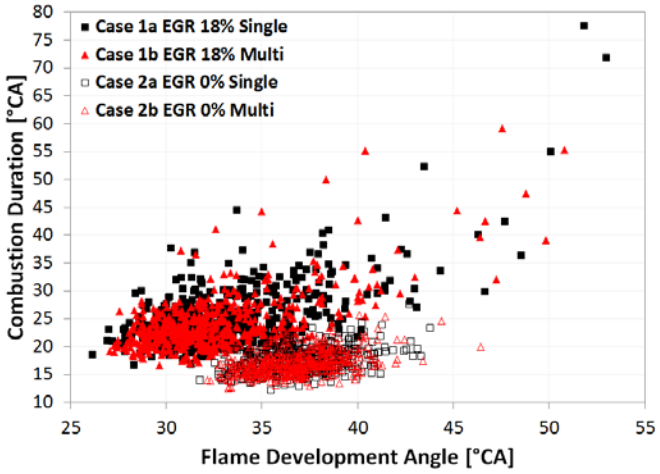

Figure 38 Effect of ignition characteristics on combustion stability for stoichiometric and dilute operations, experimental dataset

Summary/Conclusions

In this paper, multi-cycle RANS simulations were performed to investigate the combustion process in a single-cylinder GDI research engine under EGR-dilute as well as non-dilute operation. The numerical results are compared to the experimental data for selected operating conditions highlighting the effect of diluent mass on combustion stability. Main conclusions can be drawn as follows:

- RANS multi-cycle simulations show cyclic variability which comes from the variability of the large flow structures from one cycle to the next.
- Simulations using static fine mesh and detailed cold-flow analysis show that the variability of the flow from one cycle to the next is an intrinsic feature of engine multi-cycle simulations and is not a numerical artifact, nor the effect of the AMR algorithm.
- More stable cases show narrow fluctuations of the numerical trace, which is closer to what is expected from RANS. Less stable cases show large pressure fluctuations that yet correlate well with experiments.
- While CCV is not expected using RANS, this is the effect of low numerical viscosity achieved in this study using locally fine grid and high order of numerics.

- The simple case of a cylinder in cross flow demonstrates that numerical viscosity has significant impact on the trade-off between repeatability and accuracy. Even more importantly, it demonstrates that unsteady RANS does not necessarily deliver an ensemble-average result.

- The choice of the specific combustion model does not affect the numerical predictions in terms of cyclic variability. Two different combustion models (SAGE, direct chemistry approach, and G-Equation, flamelet approach) are used to describe dilute combustion. They both deliver the same degree of cyclic variability. They both can deliver more repeatable, although less accurate solution if numerical viscosity is increased.

- Qualitative comparison between multi-cycle RANS results and engine data for selected operating conditions shows that the CFD methodology used in this study is capable of capturing typical stability features in SI engines. It is even capable to capture the effect of specific engine parameters (ignition profile) on combustion stability for both stoichiometric non-dilute and EGR dilute conditions.

- Overall, although less accurate than LES, RANS can capture similar combustion stability features. This makes RANS an effective tool to evaluate combustion systems that are characterized by large CCV and low combustion stability, like in the case of dilute SI combustion.

Acknowledgments

The submitted manuscript has been created by UChicago Argonne, LLC, Operator of Argonne National Laboratory ("Argonne"). Argonne, a U.S. Department of Energy Office of Science laboratory, is operated under Contract No. DE-AC02-06CH11357. The U.S. Government retains for itself, and others acting on its behalf, a paid-up nonexclusive, irrevocable worldwide license in said article to reproduce, prepare derivative works, distribute copies to the public, and perform publicly and display publicly, by or on behalf of the Government.

This research is funded by DOE's Vehicle Technologies Program, Office of Energy Efficiency and Renewable Energy. The authors would like to express their gratitude to Gurpreet Singh and Leo Breton, program managers at DOE, for their support. The research engine used to run these experiments was provided by Ford Motor Company. Special thanks to Brad Boyer and Steven Wooldridge and their team from Ford Motor Company for their guidance and support.

Numerical simulations were run on the Blues Cluster at the LCRC, Argonne National Laboratory. Special thanks to Ray Bair and John Valdes for their help in facilitating the simulation work.

Contact Information

Riccardo Scarcelli, Ph.D.

Engine and Emissions Research Engineer

Center for Transportation Research, Argonne National Laboratory

rscarcelli@anl.gov

Definitions/Abbreviations

AMR	Adaptive Mesh Refinement
ANL	Argonne National Laboratory
ATDC	After Top Dead Center
CA	Crank Angle
CCV	Cycle-to-Cycle Variations
CFD	Computational Fluid Dynamics
COV	Coefficient of Variation
DEIS	Directed Energy Ignition System
DI	Direct Injection
DOI	Duration of Injection
EGR	Exhaust Gas Recirculation
ER	Equivalence Ratio
EVC	Exhaust Valve Closing
EVO	Exhaust Valve Opening
GDI	Gasoline Direct Injection
ICEs	Internal Combustion Engines
IMEP	Indicated Mean Effective Pressure
IVC	Intake Valve Closing
IVO	Intake Valve Opening
LES	Large Eddy Simulations
LLNL	Lawrence-Livermore National
MOP	Maximum Open Point
OEM	Original Equipment Manufacturer
PFI	Port Fuel Injection
RANS	Reynolds Averaged Navier-Stokes
RNG	Re-Normalization Group
RPM	Revolutions per Minute
SA	Spark Advance
SI	Spark Ignition
SOI	Start of Injection
TDC	Top Dead Center
TCI	Turbulence/Chemistry Interaction
TKE	Turbulent Kinetic Energy

References

[1] Alger, T. and Mangold, B., "Dedicated EGR: A New Concept in High Efficiency Engines", SAE Int. J. Engines 2(1):620-631, 2009.

[2] Matthias, N., Wallner, T., and Scarcelli, R., "Analysis of Cyclic Variability and the Effect of Dilute Combustion in a Gasoline Direct Injection Engine", SAE Int. J. Engines 7(2), 2014.

[3] Vermorel, O., Richard, S., Colin, O., Angelberger, C., Benkenida, A., Veynante, D., "Multi-Cycle LES Simulations of Flow and Combustion in a PFI SI 4-Valve Production Engine", SAE Technical Paper 2007-01-0151, 2007.

[4] Enaux B., Granet V., Vermorel O., Lacour C., Pera C., Angelberger C., et al., "LES study of cycle-to-cycle variations in a spark ignition engine", Proceedings of the Combustion Institute, Vol. 33, pp. 3115-3122, 2011.

[5] Granet V., Vermorel O., Lacour C., Enaux B., Dugue´ V., Poinsot T., "Large-Eddy Simulation and experimental study of cycle-to-cycle variations of stable and unstable operating points in a spark ignition engine", Combust. Flame 159, 4, 1562-1575, 2012.

[6] Tatschl, R., Bogensperger, M., Pavlovic, Z., Priesching, P. et al., "LES Simulation of Flame Propagation in a Direct-Injection SI-Engine to Identify the Causes of Cycle-to-Cycle Combustion Variations", SAE Technical Paper 2013-01-1084, 2013.

[7] Koch, J., Schmitt, M., Wright, Y., Steurs, K. et al., "LES Multi-Cycle Analysis of the Combustion Process in a Small SI Engine", SAE Int. J. Engines 7(1), 2014.

[8] Fontanesi, S., Paltrinieri, S., d'Adamo, A., Duranti, S., "Investigation of boundary condition and field distribution effects on the cycle-to-cycle variability of a turbocharged GDI engine using LES", Oil & Gas Sci. Tech., doi: 10.2516/ogst/2013142, 2014.

[9] Goryntsev, D., Nishad, K., Sadiki, A., and Janicka, J., "Application of LES for Analysis of Unsteady Effects on Combustion Processes and Misfires in DISI Engine", Oil & Gas Sci. Tech., DOI: 10.2516/ogst/2013125, 2014.

[10] Heywood, J. B., "Internal Combustion Engine Fundamentals," McGraw-Hill, 1988.

[11] Givler, S.D., Raju, M., Pomraning, E., Senecal, P.K., Salman, N., Reese II, R.A., "Gasoline Combustion Modeling of Direct and Port-Fuel Injected Engines, using a Reduced Chemical Mechanism", SAE Technical Paper 2013-01-1098, 2013.

[12] Scarcelli, R., Matthias, N.S., and Wallner, T., "Numerical Investigation of Combustion in a Lean Burn Gasoline Engine", SAE Technical Paper 2013-24-0029, 2013.

[13] Scarcelli, R., Matthias, N.S., and Wallner, T., "Numerical and Experimental Analysis of Ignition and Combustion Stability in EGR Dilute GDI Operation", ASME Paper ICEF2014-5607, 2014

[14] Richards, K.J., Probst, D., Pomraning, E., Senecal, P.K., Scarcelli, R., "The Observation of Cyclic Variation in Engine Simulations when using RANS Turbulence Modeling", ASME Paper ICEF2014-5605, 2014.

[15] Richards, K.J., Senecal, P.K., Pomraning, E., CONVERGE 2.1.0 Theory Manual, Convergent Science Inc., Madison, WI, 2013.

[16] Reitz, R. and Diwakar, R., "Structure of High-Pressure Fuel Sprays", SAE Technical Paper 870598, 1987.

[17] Schmidt, D. P. and Rutland, C. J, "A New Droplet Collision Algorithm", Journal of Computational Physics, 164, 62-80, 2000.

[18] Liu, A., Mather, D., and Reitz, R., "Modeling the Effects of Drop Drag and Breakup on Fuel Sprays", SAE Technical Paper 930072, 1993.

[19] Amsden, A. A., O'Rourke, P. J. and Butler, T. D., "KIVA-II: A Computer Program for Chemically Reactive Flows with Sprays", Los Alamos National Laboratory Report No. LA- 11560-MS, 1989.

[20] Yang, X., Solomon, A., Kuo, T.-W., "Ignition and Combustion Simulations of Spray-Guided SIDI Engine using Arrhenius Combustion with Spark-Energy Deposition Model", SAE Technical Paper 2012-01-0147, 2012.

[21] Pomraning, E., Richards, K., and Senecal, P., "Modeling Turbulent Combustion Using a RANS Model, Detailed Chemistry, and Adaptive Mesh Refinement", SAE Technical Paper 2014-01-1116, 2014.

[22] Borghi, R., Destriau, M., "Combustion and flames, chemical and physical principles, Editions Technip, Paris, 1998.

[23] Raju, M., Wang, M., Dai, M., Piggott, W., Flowers, D., "Acceleration of Detailed Chemical Kinetics Using Multi-zone Modeling for CFD in Internal Combustion Engine Simulations", SAE Technical Paper 2012-04-16, 2012.

[24] Peters, N., Turbulent Combustion, Cambridge University Press, 2000.

[25] Ewald, J. and Peters, N., "A Level Set Based Flamelet Model for the Prediction of Combustion in Spark Ignition Engines," 15th International Multidimensional Engine Modeling User's Group Meeting, Detroit, MI, 2005.

[26] Gulder, Omer L., "Correlations of Laminar Combustion Data for Alternative S.I. Engine Fuels", SAE 841000, 1984.

[27] Scarcelli, R., Wallner, T., Sevik, J., Richards, K., Pomraning, E., Senecal, P.K.,"Capturing Cyclic Variability in EGR Dilute SI Combustion using Multi-Cycle RANS", ASME Paper ICEF2015-1045, 2015.